



HAL
open science

Extreme biomimetics: Preservation of molecular detail in centimeter-scale samples of biological meshes laid down by sponges

Iaroslav Petrenko, Adam P. Summers, Paul Simon, Sonia Żóltowska-Aksamitowska, Mykhailo Motylenko, Christian Schimpf, David Rafaja, Friedrich Roth, Kurt Kummer, Erica Brendler, et al.

► To cite this version:

Iaroslav Petrenko, Adam P. Summers, Paul Simon, Sonia Żóltowska-Aksamitowska, Mykhailo Motylenko, et al.. Extreme biomimetics: Preservation of molecular detail in centimeter-scale samples of biological meshes laid down by sponges. *Science Advances* , 2019, 5 (10), pp.eaax2805. 10.1126/sci-adv.aax2805 . hal-02306377

HAL Id: hal-02306377

<https://hal.science/hal-02306377>

Submitted on 19 Nov 2021

HAL is a multi-disciplinary open access archive for the deposit and dissemination of scientific research documents, whether they are published or not. The documents may come from teaching and research institutions in France or abroad, or from public or private research centers.

L'archive ouverte pluridisciplinaire **HAL**, est destinée au dépôt et à la diffusion de documents scientifiques de niveau recherche, publiés ou non, émanant des établissements d'enseignement et de recherche français ou étrangers, des laboratoires publics ou privés.



Distributed under a Creative Commons Attribution - NonCommercial 4.0 International License

MATERIALS SCIENCE

Extreme biomimetics: Preservation of molecular detail in centimeter-scale samples of biological meshes laid down by sponges

Iaroslav Petrenko¹, Adam P. Summers², Paul Simon³, Sonia Żółtowska-Aksamitowska^{1,4}, Mykhailo Motylenko⁵, Christian Schimpf⁵, David Rafaja⁵, Friedrich Roth⁶, Kurt Kummer⁷, Erica Brendler⁸, Oleg S. Pokrovsky^{9,10}, Roberta Galli¹¹, Marcin Wysokowski^{1,4}, Heike Meissner¹², Elke Niederschlag¹³, Yvonne Joseph¹, Serguei Molodtsov^{6,14,15}, Alexander Ereskovsky^{16,17}, Viktor Sivkov¹⁸, Sergey Nekipelov^{18,19}, Olga Petrova^{18,19}, Olena Volkova²⁰, Martin Bertau²¹, Michael Kraft²¹, Andrei Rogalev⁷, Martin Kopani²², Teofil Jesionowski^{4*}, Hermann Ehrlich^{1*}

Fabrication of biomimetic materials and scaffolds is usually a micro- or even nanoscale process; however, most testing and all manufacturing require larger-scale synthesis of nanoscale features. Here, we propose the utilization of naturally prefabricated three-dimensional (3D) spongin scaffolds that preserve molecular detail across centimeter-scale samples. The fine-scale structure of this collagenous resource is stable at temperatures of up to 1200°C and can produce up to 4 × 10-cm-large 3D microfibrinous and nanoporous turbostratic graphite. Our findings highlight the fact that this turbostratic graphite is exceptional at preserving the nanostructural features typical for triple-helix collagen. The resulting carbon sponge resembles the shape and unique microarchitecture of the original spongin scaffold. Copper electroplating of the obtained composite leads to a hybrid material with excellent catalytic performance with respect to the reduction of *p*-nitrophenol in both freshwater and marine environments.

INTRODUCTION

Extreme biomimetics is the search for natural sources of engineering inspiration that leads to solutions that are well outside the human comfort zone (1). The idea is to create inorganic-organic hybrid composites resistant to harsh chemical and thermal microenvironments, templated by thermostable and chemically resistant biopolymers with naturally prefabricated three-dimensional (3D) architecture. Marine sponges have been a productive model system in the development of novel hierarchically structured 3D composites using renewable, nontoxic, and biodegradable organic scaffolds (2, 3). Over 600 million years of evolution, marine demosponges have produced constructs ranging from centimeter to meter scales (4). The gross morphology and dimensions (up

to 70 cm in diameter; see fig. S1) of proteinaceous, spongin-based 3D skeletons have been known since ancient times as bath sponges or commercial sponges. With a US\$20 million annual market volume and extensive marine farming of sponges worldwide, applications of sponges have been largely restricted to cosmetic uses (4).

Spongin, the main fibrous component of the sponge skeleton, is in the “collagen suprafamily” (5), which is still a focus of science due to its unusual, hierarchical, nanofibrillar organization (6, 7); biomechanical behavior (8); and potential for materials engineering (9). The structure of collagen-like spongin has multiple levels comprising single fibers up to 100 μm thick, composed of nanofibers, which are combined into complex hierarchical 3D networks of high macroporosity (Fig. 1A) exhibiting specific structural and mechanical properties [for review, see (4)]. In view of spongin’s thermostability up to 360°C and its resistance to acids, spongin-based scaffolds have recently been used in hydrothermal synthesis reactions aimed at developing novel Fe₂O₃- and TiO₂-based composites for electrochemical and catalytic purposes (2). Preliminary experiments on the carbonization of spongin scaffolds at 650°C have demonstrated their mechanical stability and excellent chemical functionalization, allowing their use in the design of an effective centimeter-scale MnO₂-based supercapacitor (2).

The idea of fabricating carbon materials with controlled microstructure and morphology, especially at large scales and from renewable and biodegradable natural sources, is a current trend in materials science. However, original carbon fiber materials are relatively expensive to obtain, and this can become a limiting factor in the development of 3D carbon fiber-based structures on a large scale (10). Although hydrothermal treatment of diverse proteins usually induces their decomposition without forming carbonaceous materials (11), such structural fiber-based proteins as keratin (12) and collagen (13) as well as silk (14, 15) have been reported as suitable for carbonization between 200° and 800°C, and in some cases even up to 2800°C (16). However, with the exception of some millimeter-scale silk nanofiber membranes (15) and up to 2-cm-large flexible carbonized silk worm cocoons (14), there

¹Institute of Electronics and Sensor Materials, TU Bergakademie Freiberg, Freiberg, Germany. ²Department of Biology, University of Washington, Seattle, WA, USA. ³Max Planck Institute for Chemical Physics of Solids, Dresden, Germany. ⁴Institute of Chemical Technology and Engineering, Faculty of Chemical Technology, Poznan University of Technology, Poznan, Poland. ⁵Institute of Materials Science, TU Bergakademie Freiberg, Freiberg, Germany. ⁶Institute of Experimental Physics, TU Bergakademie Freiberg, Freiberg, Germany. ⁷European Synchrotron Radiation Facility (ESRF), Grenoble, France. ⁸Institute of Analytic Chemistry, TU Bergakademie Freiberg, Freiberg, Germany. ⁹Geosciences Environment Toulouse, University of Toulouse, Toulouse, France. ¹⁰BIO-GEO-CLIM Laboratory, Tomsk State University, Tomsk, Russia. ¹¹Clinical Sensing and Monitoring, Department of Anesthesiology and Intensive Care Medicine, TU Dresden, Dresden, Germany. ¹²Faculty of Medicine and University Hospital Carl Gustav Carus of TU Dresden, Dresden, Germany. ¹³Institute for Nonferrous Metallurgy and Purer Materials, TU Bergakademie Freiberg, Freiberg, Germany. ¹⁴European XFEL GmbH, Schenefeld, Germany. ¹⁵ITMO University, St. Petersburg, Russia. ¹⁶Institut Méditerranéen de Biodiversité et d’Ecologie (IMBE), CNRS, IRD, Aix Marseille Université, Avignon Université, Station Marine d’Endoume, Marseille, France. ¹⁷Department of Embryology, Faculty of Biology, Saint-Petersburg State University, Saint Petersburg, Russia. ¹⁸Institute of Physics and Mathematics, Komi Science Center Urd RAS, Syktyvkar, Russia. ¹⁹Pitirim Sorokin Syktyvkar State University, Syktyvkar, Russia. ²⁰Institute of Iron and Steel Technology, TU Bergakademie Freiberg, Freiberg, Germany. ²¹Institute of Technical Chemistry, TU Bergakademie Freiberg, Freiberg, Germany. ²²Institute of Medical Physics, Biophysics, Informatics and Telemedicine, Faculty of Medicine, Comenius University, Bratislava, Slovakia.

*Corresponding author. Email: teofil.jesionowski@put.poznan.pl (T.J.); hermann.ehrlich@esm.tu-freiberg.de (H.E.)

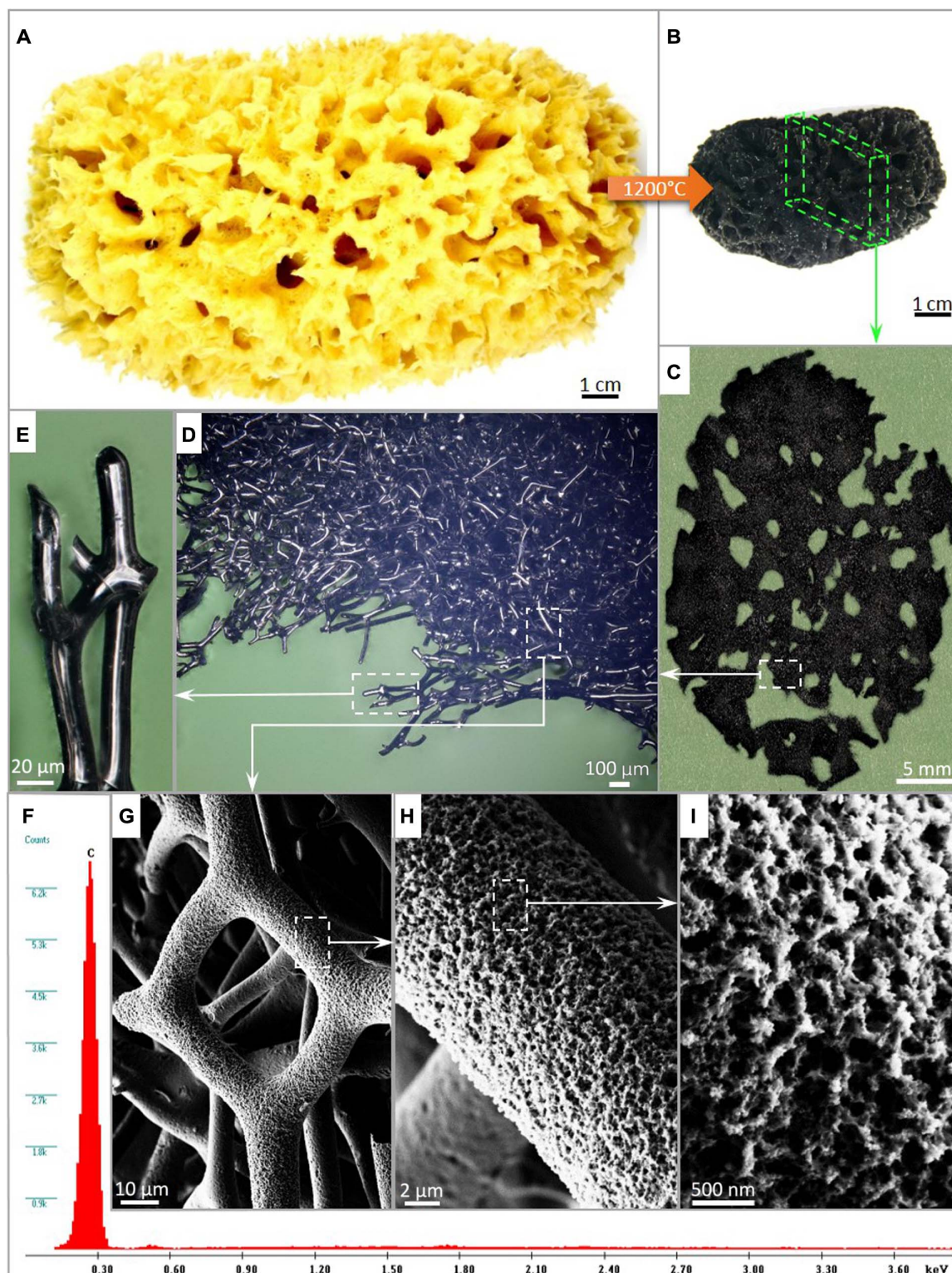


Fig. 1. Overview of the transformation of spongin scaffolds to a carbonized 3D structure at 1200°C. (A) Typical cellular and hierarchical morphology of *Hippospongia communis* demosponge organic skeleton after purification remains unchanged during the process of carbonization in spite of a decrease in volume by up to 70%. (B) Carbonized 3D scaffold can be sawn into 2-mm-thick slices (C). Both stereomicroscopy (D and E) and SEM images (G and H) of carbonized spongin network confirm its structural integrity, typical for sponge-like constructs. However, the surface of carbonized fibers became rough (H) due to the formation of abundant nanopores (I) (see also fig. S9). The EDX analysis of purified carbonized spongin (F) provides strong evidence of its carbonaceous origin. Photo credit: Iaroslav Petrenko and Michael Kraft, TU Bergakademie Freiberg.

are no reports on sponge-like and ready-to-use carbon scaffolds with hierarchical pores and 3D-connected skeletons. A sponge analog from the plant world, *Luffa* sp. (17) has been used as a pattern, but despite visual similarity with the sponge-like networks of xylem fibers of dried *Luffa* fruit, this biomaterial has several disadvantages. After carbonization, *Luffa* fibers with diameters in the range of 150 to 450 μm broke and the network structure collapsed, losing all the higher-level architecture. Only carbonized material from the plant in the form of powder has been used for further applications (17). Similar results have been reported concerning carbon fibers obtained from silk, which were partially melted and too fragile to handle (18). The combination of hierarchical complexity ranging from nanometers to centimeters and the ease of culture in arbitrary shapes and sizes motivated us to develop new 3D carbonized spongin scaffolds capable of withstanding temperatures as high as 1200°C without loss of nanoscale architecture. We hypothesized that spongin could be converted to carbon at high temperatures without loss of its form or structural integrity and that its specific surface area would increase due to the appearance of nanopores, favoring its further functionalization as a catalyst. Here, we report the first successful effort to design a centimeter-scale 3D carbonized spongin-Cu/Cu₂O material using an extreme biomimetics strategy, and demonstrate the ability of this material to effectively catalyze the reduction of 4-nitrophenol (4-NP) to 4-aminophenol (4-AP) in both marine and freshwater environments.

RESULTS

Carbonization of spongin scaffold and its structural characterization

We carbonized spongin scaffolds by directly heating purified sponge skeletons (Fig. 1) at 1200°C for 1 hour under Ar flow (see Materials and Methods). Carbonized spongin scaffolds maintained their fibrous 3D morphology in spite of a decrease in total volume by around 70%. The diameter of spongin fibers during carbonization and the pore size within the fibrous network decreased from $16 \pm 1 \mu\text{m}$ to $8 \pm 1 \mu\text{m}$ and from 97 to 235 μm to 28 to 140 μm , respectively. However, the density of carbonized spongin increased up to $0.1119 \pm 0.001 \text{ g/cm}^3$ in comparison with native spongin ($0.0328 \pm 0.002 \text{ g/cm}^3$). There is an increase in the Brunauer-Emmett-Teller (BET) specific surface area of carbonized spongin fibers up to $425 \pm 30 \text{ m}^2/\text{g}$ in comparison with their native form ($3.45 \pm 0.32 \text{ m}^2/\text{g}$) due to the development of highly mesoporous surfaces (Fig. 1, H and I and fig. S3). In contrast to the fragile carbonized scaffolds obtained from other natural biomaterials, carbonized spongin can be sawn into slices up to 2 mm thick using a metallic saw with a blade thickness of 1.5 mm (see fig. S4A). The measured compression strength of carbonized spongin was 1.3 MPa at a density of 0.1119 g/cm^3 (see fig. S4B), which is higher than that of carbon foam samples with kaolinite additions carbonized at 1200°C (19) and is comparable to that of graphite foams derived from coal-tar pitch (20).

The carbonaceous material was initially analyzed using solid-state ¹³C nuclear magnetic resonance (NMR) spectroscopy (fig. S6) with the aim of understanding its structural chemistry. By comparison of our ¹³C NMR results (fig. S6) with those previously published (21), we found that the material resembles amorphous graphite but can also contain amounts of ordered, graphite-like domains. To confirm this finding, we used x-ray diffraction (XRD) and Raman spectroscopy, which are useful for characterization of the ordered-disordered state of carbonized materials (16).

The measured XRD patterns of the carbonized spongin samples are shown in Fig. 2A. The peaks are broad, and only the strong 002 ($2\theta \approx 25^\circ$), 100 ($2\theta \approx 43^\circ$), and 112 ($2\theta \approx 80^\circ$) peaks may be reliably distinguished in the pattern. XRD lines 100 and 112 are strongly right-hand asymmetric. Similar peak shapes have been described for turbostratically disordered carbon, obtained, for example, by high-temperature treatment of high-melting point coal-tar synthetic pitch (23). The quantitative extraction of microstructure parameters from powder diffraction patterns of turbostratically disordered materials has been extensively discussed for diverse materials including carbon (22). We used the fundamental Dopita *et al.* (22) approach as implemented in the MStruct routine (23), which was developed for quantitative description of the microstructure of carbon samples.

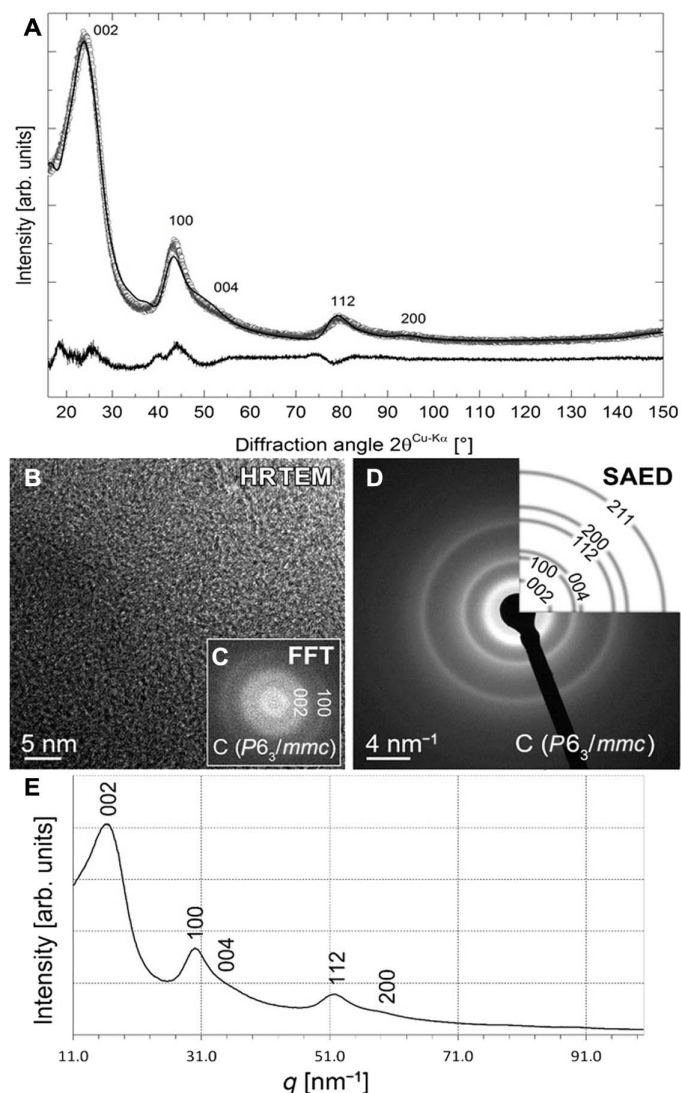


Fig. 2. Identification of carbonized spongin as turbostratic graphite. XRD analysis of spongin carbonized at 1200°C. (A) Circles, measured data; solid line, calculation according to the method described (25) and values given in table S1; bottom line, difference between measured and calculated intensities. Labels are the diffraction indices *hkl*. (B) HRTEM image with corresponding indexed FFT (C). (D) SAED pattern for carbonized spongin and corresponding 1D intensity distribution (E) as the sum of intensities along the diffraction rings.

The turbostratic graphite obtained from spongin was also confirmed using high-resolution transmission electron microscopy (HRTEM) (Fig. 2B), fast Fourier transformation (FFT) (Fig. 2C), and selected-area electron diffraction (SAED) (Fig. 2D). The results of the integral (XRD; Fig. 2A) and local (SAED; Fig. 2E) diffraction methods show agreement with respect to the formation of turbostratic graphite. In addition, the measured electron energy-loss spectroscopy (EELS) spectra of carbonized spongin correspond with previously published data (24).

Turbostratic disorder means that the sp^2 -hybridized sheets of graphite, the (001) planes, are mutually shifted along the a and b directions and rotated around the normal of the graphite sheets (i.e., around the c axis). The approach of Dopita *et al.* (22) interprets the structure in terms of the following variables: the mean lattice parameters of graphite (space group $P6_3/mmc$), a_0 and c_0 ; the size of largely undistorted entities (clusters) along the a and c directions (L_a and L_c) and their variations (v_a and v_c) as a log-normal distribution; and the mean atomic displacements along a and c ($\langle u_a^2 \rangle$ and $\langle u_c^2 \rangle$). The values obtained from a least squares refinement are listed in table S1. The microstructure parameters of the turbostratic carbon obtained from XRD suggest that the turbostratically disordered carbon is organized in nanoclusters with a lateral size of approximately 3 nm and a thickness of 1 nm (i.e., three atomic layers along c). These nanoclusters are stable at very high temperatures (25, 26). As expected for graphitic structures with much weaker bonding between the (001) sheets, the structural disorder is higher along the c direction ($\langle u_c^2 \rangle$) than within the tightly bound a - b plane ($\langle u_a^2 \rangle$). Another well-known feature of these heavily distorted carbon structures is a strongly expanded lattice parameter c , which is a result of the nonperfect stacking of the layers. The lattice expansion and the structural disorder in the c direction are frequently related to the presence of impurities “intercalated” between the lattice planes (001) (27).

On the nanoscale, the graphite nanoclusters produce a porous structure. The TEM micrograph of the carbonized spongin, a collagen-based fibrillar protein (4), is shown in Fig. 3. At the middle-resolution regime, nanometer-thin fibrils are detected (see arrows in Fig. 3A). The Fourier transform displays diffraction maxima of 2.45 nm^{-1} corresponding to a direct-space distance of 8.16 \AA and diffraction maxima of 0.78 nm^{-1} corresponding to a spacing of 25.6 \AA . These direct-space spacings do not occur in the main allotropes of carbon: crystalline graphite or diamond. Formally, 8.16 \AA might correspond to the (111) lattice planes of C_{60} ; however, much larger lattice planes over 25 \AA are also present at the same time. Because the largest lattice planes allowed C_{60} amounts to 14.04 \AA , we exclude this possibility and consider patterns corresponding to variants of graphitic foam. This kind of carbon may build up differently sized lattices depending on aromatic spacers (phenyl groups) between sp^3 blocks, giving rise to porous structures (28). The rectangle at the center is further enlarged in Fig. 3B. In the enlarged image, nanostructures appear with pearl-like chains with periodicities corresponding to 2.86 nm (Fig. 3B). Similar spacings are found in collagen, bearing a strong resemblance to the periodic unit along the fibril long axis of the triple helix (29, 30). Comparison between native and carbonized spongin is presented in fig. S5. Registered images show that the nanofibers and triple helices are nevertheless observed in both samples, meaning that the structural features of collagen helix are preserved after carbonization of spongin at 1200°C .

At a higher magnification, in selected regions, nanostructuring could be observed, giving rise to a periodic pattern on the nanoscale (see Fig. 3C). The Fourier transform of the image reveals a hexagonal lattice (top left inset), where the reflections correspond to a spacing of 4.5 nm . To be

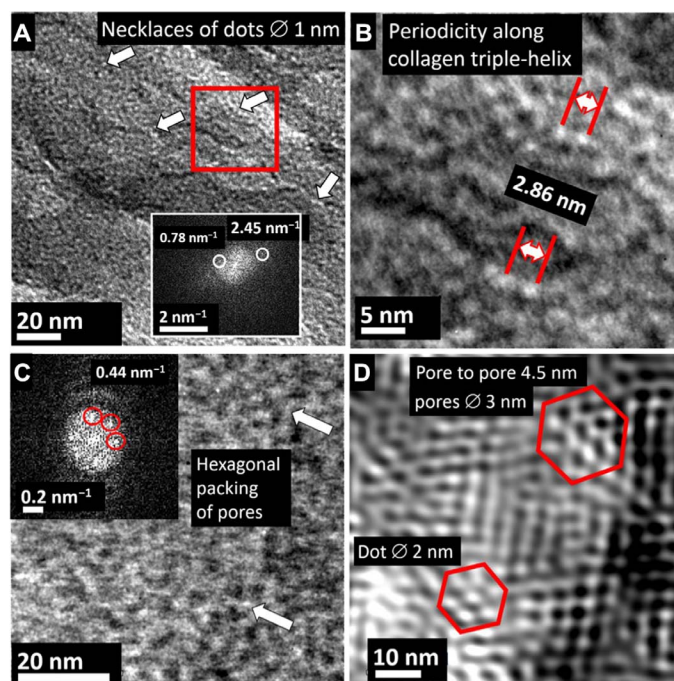


Fig. 3. TEM images of 80-nm-thin cuts of spongin carbonized at 1200°C . (A) Overview image of carbonized spongin consisting mainly of collagen nanofibrils. Arrows indicate pearl necklace structures being parallel to each other. The red frame indicates the enlarged region taken for image (B). In the Fourier transform, diffraction maxima corresponding to the direct-space distances of 8.16 and 25.6 \AA are recorded. (B) Enlarged image of the nanostructures. Pearl-like chains appear showing periodicities of 2.86 nm , which is typical for the triple helix periodicity of collagen along the fibril long axis. (C) The enlarged region reveals nanodot-like structures with nanopore inclusions. The Fourier transform shows a regular hexagonal pattern (top left inset) with a 4.5-nm periodicity. (D) Fourier-filtered image of (C). For filtering, the reflections of the Fourier transform corresponding to 0.44 nm^{-1} were selected corresponding to a spacing of 4.5 nm , as indicated in the inset. In the processed micrograph, hexagonal structures are observed with a pore-to-pore distance of 4.5 nm and pore diameters of about 3 nm (top left).

able to interpret the features in the HRTEM micrograph in Fig. 3C, we applied a Fourier filtering in the region shown in Fig. 3C by masking out the reflections corresponding to a reciprocal space distance of 0.44 nm^{-1} or a lattice spacing of 4.5 nm in bright field. The filtering process emphasizes the hexagonal pattern consisting of dark, pore-like regions on the nanometer scale. At the same time, a hexagonal pattern of dots, appearing as bright spots, is observed. Thus, heating leads to the transformation of collagen-based spongin into a hexagonal carbon structure (Fig. 3C). Simultaneously, structures with periodicities characteristic for the collagen triple helix are recorded (Fig. 3B) (30).

The structural and chemical changes after carbonization were investigated using Raman spectroscopy, x-ray photoelectron spectroscopy (XPS), and near-edge x-ray absorption fine structure (NEXAFS) spectroscopy.

Raman spectra at different temperatures show the D, G, and 2D bands. The position and intensity of the D and G bands, as well as the D/G band intensity, were retrieved by means of a mixed Gaussian-Lorentzian fitting model (Fig. 4, fig. S7, and table S2). The D band shifts toward lower energy and the G band shifts toward higher energy with increasing treatment temperature. Following the model of Ferrari and Robertson (31), this change indicates increasing clustering and the presence of sp^2 chains. More precisely, we can say that the material evolves

from amorphous carbon toward nanocrystalline graphite and presents mixed sp^2 and sp^3 sites. The average graphite nanocrystallite size L_a is inversely proportional to the intensity ratio of the D and G bands according to the experimental equation $I(D)/I(G) = C(\lambda)/L_a$ (31), where $C \approx 16$ nm for near-infrared laser excitation (32). In the case of spongin carbonized at 1200°C, the average graphite nanocrystallite size L_a is ≈ 3 nm, in agreement with the XRD results. XPS provides information about the elemental and chemical composition of the surface [63% of the signal originates from below 26 Å and 95% from below 78 Å (33)]. In fig. S8A, we present survey scans in the energy range between 0 and 1350 eV as a function of temperature, which show that the C 1s core-level feature consists of a main peak located at 284.5 eV that can be attributed to C—C bonds. Further, we identify a shoulder at higher binding energies (285.5 to 286.0 eV) and a weak feature around 288.4 eV, which can be attributed to C—O—C and O—C=O compo-

nents, respectively. On annealing of the sample up to 1200°C, the line-width of the main feature decreases and the two weak features become less visible, probably as a direct result of a loss of oxygen at the sample surface. This is supported by comparing the elemental composition as a function of temperature, focusing on the two main core-level peaks, C 1s and O 1s (fig. S8B). Starting from about 70 atomic % (at %) for carbon and 15 at % for oxygen on heating at 400°C, the quantity of carbon increases up to nearly 90 at % at 1200°C, whereas the quantity of oxygen decreases by more than 5 at %.

Partial NEXAFS C 1s K-edge spectra of native and carbonized spongin heated at different temperatures are shown in Fig. 4B in arbitrary units after normalization to unity at 315-eV photon energy. The 285.0-eV resonance can be ascribed to aromatic structures (π^*_{aromat}), the 287.6-eV peak to amide (N—C=O) or imine (C=N) groups, the 288.1-eV feature to the peptide group CON, the 288.6-eV maximum

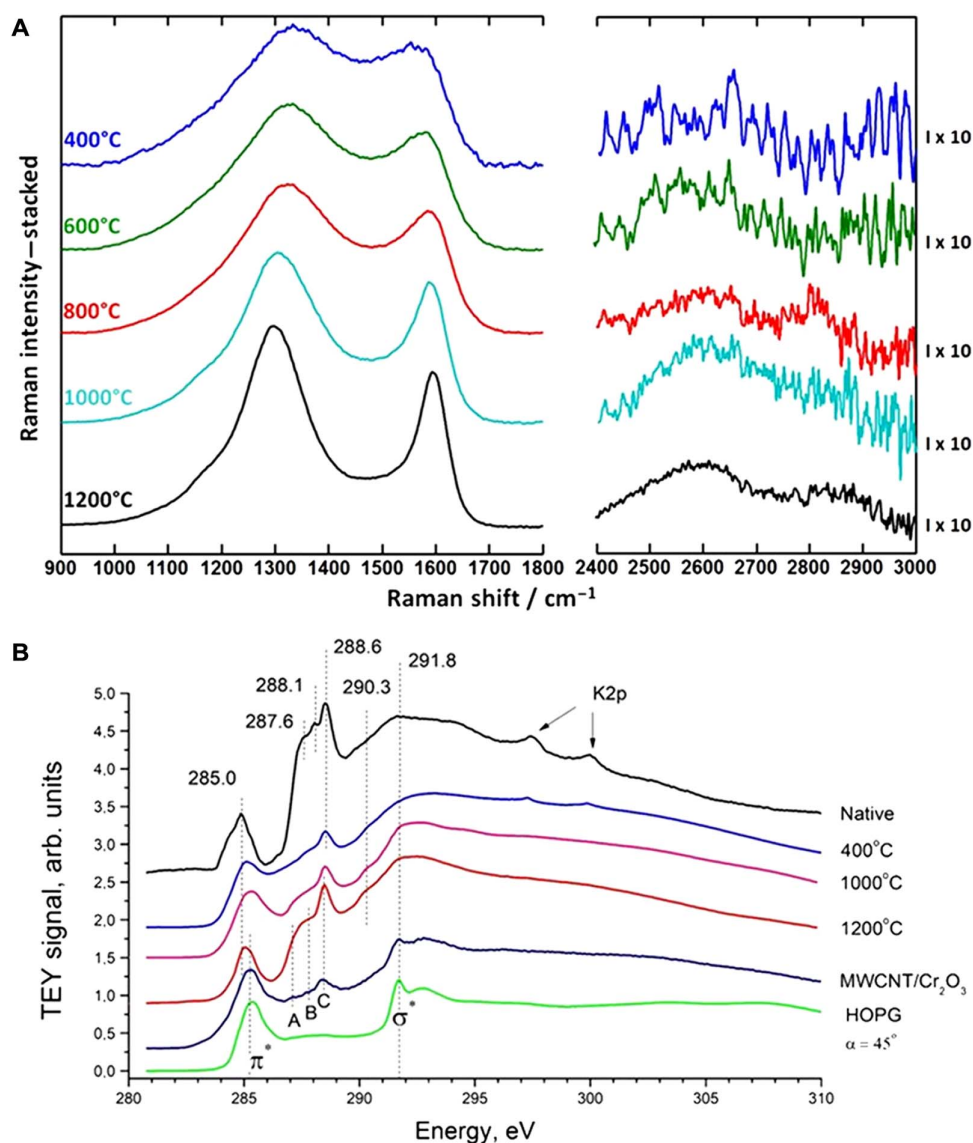


Fig. 4. Spectroscopic characterization of carbonized spongin scaffold. (A) Baseline-corrected Raman spectra of spongin carbonized at different temperatures. The intensity of the region between 2400 and 3000 cm^{-1} is multiplied by a factor of 10 for better visibility. (B) NEXAFS C 1s K-edge spectra of native and carbonized spongin heated at different temperatures, HOPG, and nanocomposite MWCNT/ Cr_2O_3 (34).

to the carboxyl group COO⁻, and the 291.6-eV-wide resonance to C 1s→σ* transitions within the various atomic groups. The structure between 297.5 and 300.0 eV can be assigned to the K 2p_{3/2}→3d and K 2p_{1/2}→3d transitions within the potassium compounds. After heating of the sample up to 1200°C, the fine structure from nitrogen and potassium compounds and the peptide bond peak completely disappear in the NEXAFS C 1s and N 1s spectra (see Fig. 4B). This indicates the absence of organic compounds within the sample, while the structure at 288.5 eV (COO) is preserved in the spectrum, and a new peak at 290.3 eV, which corresponds to the [CO₃]²⁻ anion group, appears after heating. A comparison of the C 1s spectra between native and heated (up to 1200°C) spongin reveals a 0.2-eV shift of the peak at 285.0 eV, which is characteristic for aromatic rings and hexagonal structures in graphite, respectively. This fact is clearly seen from comparison of the NEXAFS C 1s spectra of carbonized spongin after heating to 1200°C with the previously reported spectra for highly oriented pyrolytic graphite (HOPG) and multiwalled carbon nanotubes (MWCNTs) covered by a nanosized chromium oxide layer (34). This is correlated with Raman spectroscopy data. The structures A, B, and C presented for carbonized spongin (Fig. 4B) correspond to transitions from the C 1s level to π*-unoccupied orbitals of C—O—C, C—O, and C=O groups, respectively, and are caused by the oxidation of carbon. According to XPS data (see fig. S8), the oxides' contribution is not more than 10% of the total intensity.

Structural characterization of Cu/Cu₂O carbonized spongin scaffolds

Electrical conductivity of carbon is well recognized. We use this property to functionalize the obtained carbonized spongin scaffolds (see Fig. 1, B and C) with copper by the electroplating method (see also Materials and Methods). After electroplating with copper for 30 s, the 3D carbonized scaffold resembles the shape and architecture of the initial material before metallization (Fig. 5, A and B, and fig. S9). Furthermore, the carbonized scaffold remained stable after 12 hours of sonication at room temperature. The BET surface area of the resulting composite, henceforth denoted as CuCSBC (Cu/Cu₂O carbonized spongin scaffolds), was measured at 83.2 ± 0.3 m²/g.

Raman spectroscopy, XPS, and x-ray absorption spectroscopy (XAS) were used to identify copper-containing phases within CuCSBC. Raman spectra were acquired at several points on the copper layer. All spectra were similar; a representative spectrum is shown in fig. S10. Two Raman bands were detected at 528 and 622 cm⁻¹, indicating that the copper layers contain a substantial fraction of copper(I) oxide (Cu₂O) (35).

A comparison of XPS survey spectra taken for the carbonized sponge annealed at 1200°C and the copper metallized sample is shown in fig. S11. These spectra show that after metallization, around 25 at % of the copper on the surface of the carbonized spongin scaffold is in the Cu(I) (Cu₂O) oxidation state.

The chemical state of copper from CuCSBC was also probed using XAS at the Cu K-edge. The detected fluorescence signal is plotted in Fig. 5C together with reference spectra of CuO and Cu₂O powder samples, as well as Cu metal foil, recorded under the same experimental conditions. The CuCSBC spectrum strongly resembles the Cu₂O spectrum in terms of both energy position and overall spectrum shape. However, the broadened peak at 8.986-keV photon energy and the shape of the undulations in the EXAFS region above 9.0 keV indicate the presence of metallic Cu. By contrast, the CuO spectrum is shifted by several electron volts toward higher energies, because the higher

oxidation state of the Cu ions gives rise to the well-known chemical shift revealed by the x-ray core-level spectroscopy. The bulk-sensitive Cu K-edge data therefore unambiguously demonstrate that, several weeks after deposition onto the carbonized spongin, the copper is mostly present in the form of copper(I) oxide, but a sizable fraction of Cu metal is still found in the samples. Local analyses of the chemical and phase composition of the metallized area of the carbonized spongin microfiber were done in an analytical TEM on a focused ion beam lamella, which was cut from a carbon microfiber that was centrally cracked during the carbonization process and filled during electroplating (Fig. 5D). The SAED pattern from the carbonized spongin region [right-hand side of the scanning transmission electron microscopy (STEM) bright-field image in Fig. 5D] confirms the presence of turbostratically disordered graphite (Fig. 5E). The SAED pattern (Fig. 5F) revealed that the broken region, which was filled during the electroplating, is almost single crystalline. The indexing of diffraction spots showed an exact match with the diffraction pattern of the Cu₂O phase crystallizing in the cubic space group *Pn3m* (see note S10). In contrast, the interface region located between the carbonized scaffold and the electroplated layer (left-hand side of Fig. 5D) contains nanocrystalline metallic copper. This result was obtained from the SAED (Fig. 5G) and combined energy-dispersive x-ray (EDX)/EELS analyses (Fig. 5, H to K), and confirmed by HRTEM/FFT analysis (Fig. 5L). The HRTEM image (Fig. 5L) shows a copper nanocrystallite with a size of 4.5 nm. The FFT of the HRTEM image confirmed the presence of metallic copper with the space group *Fm3m* and the [112] orientation along the zone axis. The analysis of an EDX line scan made across a sample area containing several nanocrystallites (Fig. 5, M and N) suggests that the copper nanocrystallites grow directly on the carbonized scaffold.

Catalytic properties of CuCSBC

The reduction reaction of 4-NP to 4-AP is of great environmental importance. 4-NP is widely used in the production of pharmaceuticals, dyes, and pesticides, and as a result, it is also a common toxic water pollutant, especially in marine ecosystems (36, 37). Currently, there is no way to catalyze the reduction of 4-NP in simulated sea water, which represents a great challenge to ecologists and environment protection agencies worldwide. The progress of the reduction of 4-NP was monitored by taking ultraviolet-visible (UV-vis) absorbance spectra every 60 s. Typically, the 4-NP water solution shows absorption maxima at 317 and 400 nm, because of the presence of the equilibrium between 4-NP (317 nm) and the 4-nitrophenolane anion (400 nm). However, this equilibrium is shifted toward the 4-nitrophenolane anion when NaBH₄ is added to the solution (for review, see note S13 and fig. S12A). In the solution of simulated sea water, only the peak at 400 nm is present (fig. S13B).

The addition of 5 mg of CuCSBC to the system leads to a reduction in the intensity of the nitrophenolate anion peak and a simultaneous increase in the peak corresponding to 4-AP at 300 nm (Fig. 6, A and B). In the case of both tested reaction conditions—simulated sea water and deionized water—the reduction was complete after 2 min, as shown by the disappearance of the band characteristic for 4-NP and discoloration of the solution (Fig. 6, A and B). Nevertheless, there was no proportional increase in the intensity of the peak characteristic for 4-AP, which may be linked to a difference in the molar extinction of 4-NP and 4-AP (36). An important part of the research was the evaluation of kinetic aspects of the reduction process. Results for reduction kinetics were calculated according to Eq. 1 (see Materials and Methods). The curves obtained are shown in Fig. 6 (C and D). The rate constants

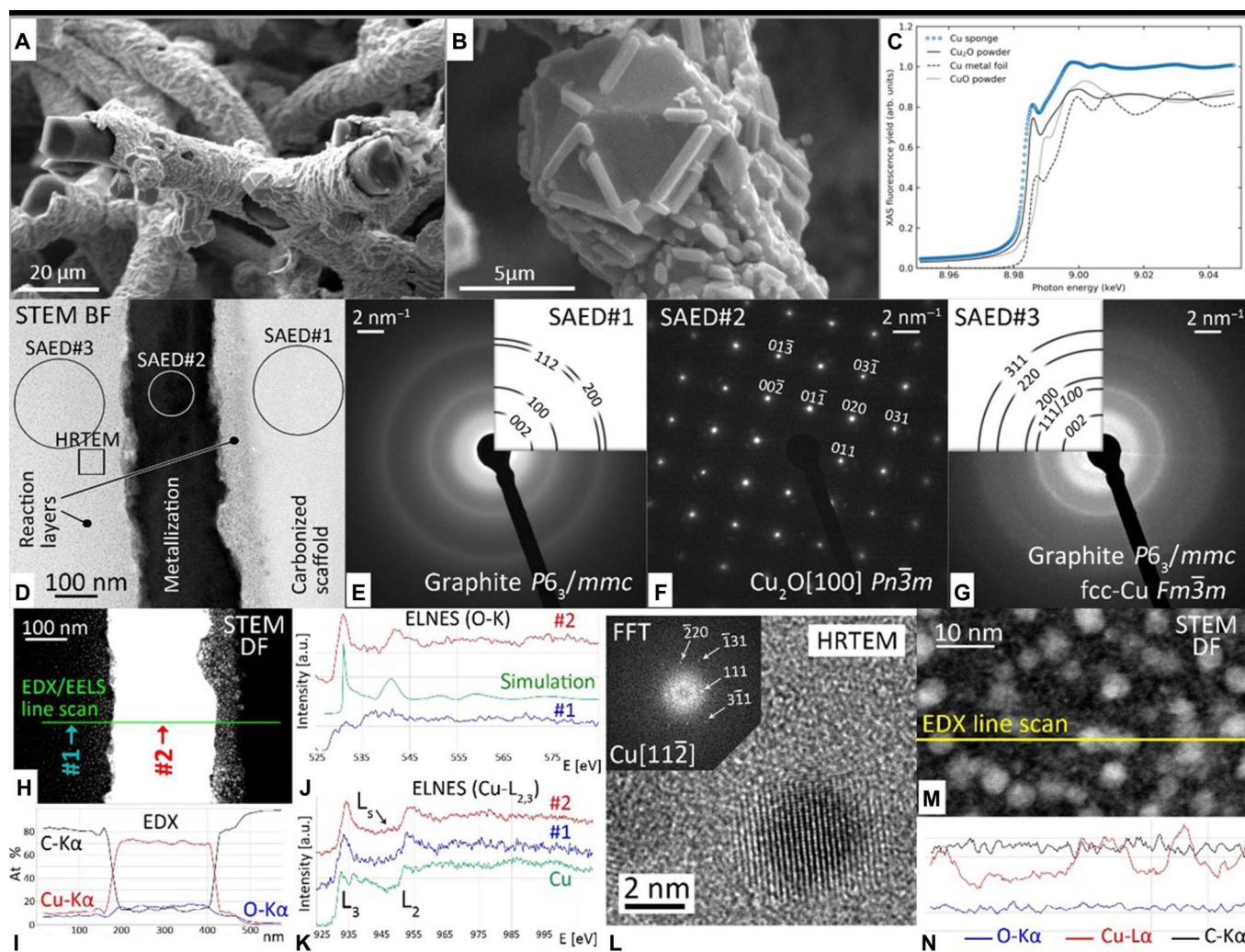


Fig. 5. Structural characterization of CuSCBC. SEM images (A and B) of the 3D carbonized scaffold after electroplating with copper and following sonication for 1 hour. The metallized scaffold has been mechanically broken to show the location of carbon microfibers. Well-developed crystals (B) can be well detected on the surface of the microcrystalline phase, which covers the carbon microfibers with a layer of up to 3 μm thick. The XAS fluorescence yield signal for the K-edge of Cu in copper layers deposited on the carbonized spongy surface is shown in comparison with reference spectra of CuO and Cu₂O standards (C). STEM bright-field (BF) overview of Cu-carbonized microfiber (D) with corresponding SAED pattern from turbostratic graphite (E), interface layer (F), and reaction layer (G). (H) STEM dark-field (DF) image with the path of the EDX/EELS line scan. (I) Concentration profiles of C, Cu, and O calculated from the EDX scan. Electron energy-loss near-edge structure (ELNES) spectra measured near the K-edge of oxygen and L-edge of copper are shown in (J) and (K), respectively. (L) HRTEM micrograph and indexed FFT of a Cu nanocrystallite. (M) Path of an EDX line scan through the reaction layer and (N) the corresponding intensity profiles of the spectral line K α of oxygen, L α of copper, and K α of carbon.

were calculated to be 0.0326 and 0.0400 s^{-1} for the reactions carried out in simulated sea water and deionized water, respectively.

DISCUSSION

It has been shown that catalytically active biomimetic materials are accessible from natural feedstock. Our study demonstrates fabrication of centimeter-large, mechanically stable carbon materials with controlled 3D microstructure and morphology using collagen-based matrices via a hybrid carbonization process in which spongy thermolysis products are coated with copper. The increase of surface area after carbonization of biological materials is well known. In our case, the naturally occurring collagen microfibril is hydrated and highly interconnected and thus polymerized. During the carbonization process of spongy, the water

and most of the volatile components are released as pyrolysis gases. The interfibrillar bonds are broken, thus releasing nanofibril structures and forming a carbonaceous backbone during heating. It is logical that the carbonized product should show a much higher specific surface area than the completely interconnected initial matrix. The nanofibers and triple helices are nevertheless observed in both samples (fig. S5), meaning that the structural features of collagen helix are preserved. It is in line with hypothesis that precursors with well-organized structures lead to the formation of ordered porous carbon. Similar effect was observed by Deng and co-workers (38). These authors used collagen to prepare well-defined carbon with enhanced surface area and preserved well-defined morphology of natural collagen fiber. However, in contrast to our study, the authors performed carbonization of collagen, which was initially fixed with selected metal ions including Zr(IV),

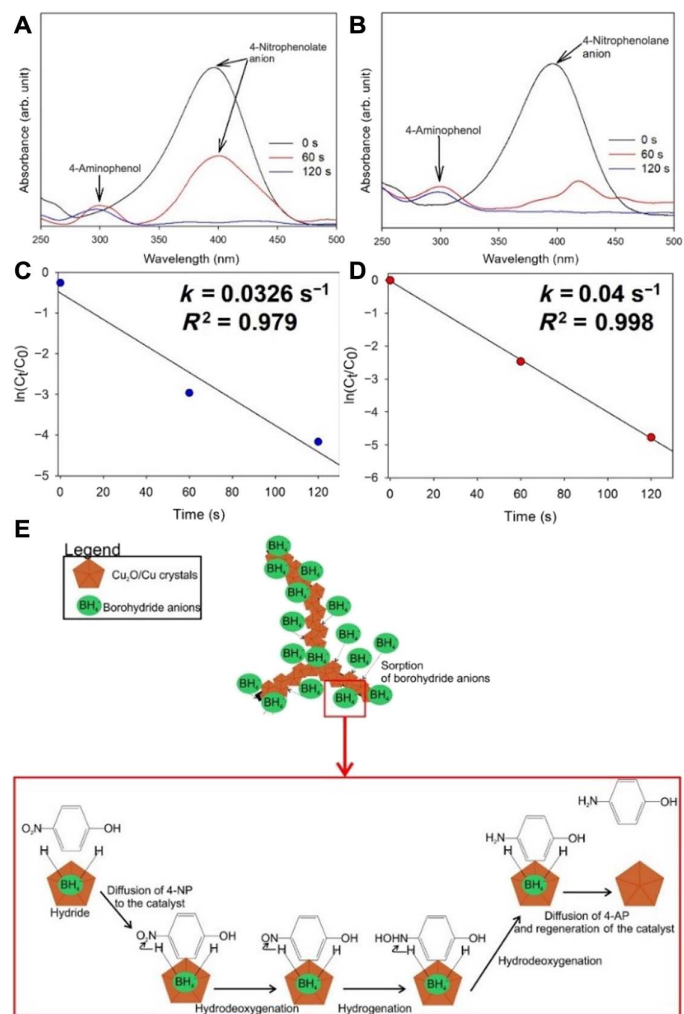


Fig. 6. Catalytic performance of CuCSBC. Transformation of 4-NP to 4-AP after addition of 5 mg of the CuCSBC catalyst (A) in simulated sea water, with (C) reaction kinetics, and (B) in deionized water, with (D) reaction kinetics. (E) Proposed mechanism of reduction of 4-NP using CuCSBC.

Cr(III), Al(III), and Fe(III). In our case, due to the unique nature of spongin fibers, this kind of “chemical stabilization” is not necessary. This remains the principal advantage of spongin in contrast to collagens from other sources. In addition, the fine surface of 3D carbon remains after functionalization with Cu/Cu₂O and can be seen on higher magnification (fig. S9).

We show the exceptional potential and stability of CuCSBC in simulated sea water at 5°C as well as in deionized water (see notes S13 to S16). We conclude that CuCSBC is a renewable and stable catalyst, which can be used for the removal of 4-NP including from contaminated marine environments. The prediction of a plausible mechanism of reduction is important to identify the catalyst’s active sites. A sorption test of 4-NP onto CuCSBC shows negligible affinity of 4-NP to the catalyst surface (see note S15). Thus, the reduction may proceed in two steps: BH⁴⁻ anions are adsorbed onto the surface of the catalyst, and afterward, a hydrogen atom is released from the hydride and reduces the 4-NP molecule (Fig. 6E). Therefore, the mechanism of reduction of 4-NP may be associated with electron transfer from the adsorbed hydride

anion to 4-NP molecules, using the metal particles as a medium. A similar mechanism was proposed by Zhang *et al.* (36), who tested the catalytic activity of Ni nanoparticles dispersed on silica nanotubes, and by Hasan *et al.* (39), who used N-doped cobalt-carbon composite. The present results suggest that the excellent catalytic performance of CuCSBC is a consequence of the presence of Cu₂O/Cu crystals on the surface of the carbonized spongin fibers and is also related to the 3D, hexagonal, and mesoporous structure of this unique biomimetic carbonaceous support (note S15).

The use of spongin for the synthesis of carbon-based materials is economically feasible, because it is a natural, renewable, and ready-to-use source that can be cultivated under marine farming conditions at large scale worldwide (4). Usually, 3D carbon-based materials obtained via direct carbonization of biomass (including raw collagen) are very fragile (38) and can be used only in the form of powder. In contrast, carbonized spongin is mechanically so robust that it can be prepared in diverse forms according to its intended use. Future research could be geared toward atomistic simulations of material and its structure, which definitely will provide additional insight into optimizing the material and can be a milestone toward more efficient bioinspired material designs (40–42).

A special property of the modified spongin fibers is the ability to conduct heat. The use of this property can be made on a large scale in heterogeneous catalysis. It has long been known that heterogeneous catalyst beds may tend to form hyperthermic islands, as a consequence of which product selectivities suffer from thermal catalyst modification. For this reason, major effort is being invested in reactor engineering with the aim of providing entirely isothermic conditions.

One such example is the reaction of syngas (CO:H₂ = 1:2) to methanol, where the heat of formation has to be eliminated effectively to avoid temperatures above 270°C. Above this value, catalysts age within hours, making it necessary to replace the entire catalyst fill. The situation is even more complex when CO₂ is hydrogenated to methanol. Here, the formation of molar fractions of water necessitates highly controlled isothermic conditions in the catalyst bed to prevent it from being deactivated (43). In view of the potential use of CO₂ hydrogenation in solving the climate change issue, catalysts that can be produced from renewable, naturally prefabricated biological materials of sponge origin may make a significant contribution to achieving these goals.

MATERIALS AND METHODS

Carbonization of spongin scaffolds

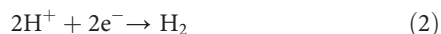
To carbonize the spongin scaffolds, selected fragments (Fig. 1A) up to 15 cm in diameter were placed in the center of a standard heating microscope device (fig. S2A). After pumping and purging the system with Ar three times, the temperature was ramped at 20°C min⁻¹ up to 1200°C with feeding of Ar (150 standard cubic centimeters per minute) at ambient pressure.

X-ray absorption spectroscopy

The Cu K-edge x-ray absorption spectra were taken at beamline ID12 of the European Synchrotron Radiation Facility (Grenoble, France). The data were obtained at room temperature by recording the total fluorescence yield signal with a photodiode mounted in a backscattering geometry. All spectra are shown normalized to the incident photon flux, which was determined using a 4-μm-thin Ti foil in the beam, upstream of the sample. The beam size was 0.3 × 0.3 mm². The data were taken several weeks after Cu deposition onto the sponge.

Copper electroplating

Spongin scaffolds carbonized at 1200°C were electrically conductive and were used as electrodes in electrochemical processes. The cathodic electrochemical processes may be described by Eqs. 1 and 2, where the prepared substrate was used as a cathode for the electrochemical deposition of Cu



The electrochemical deposition of copper was carried out in a 50-ml glass tumbler with electrolyte subject to a DC voltage of 0.2 V and a current of 0.02 A for 2 hours. The DC source was a VoltCraft PS2403D laboratory power supply (Germany) with fine control of voltage (stability, 0.5%) and current. Copper sulfate solution (0.1 M) containing sulfuric acid (4 g liter⁻¹) was used as the electrolyte.

Procedure of reduction of 4-NP to 4-AP

Typically, the reaction was carried out in a quartz cuvette with an optical path length of 1 cm and monitored using UV-vis spectroscopy (Jasco V-750, Japan) at 25°C in a scanning range of 250 to 500 nm. An aqueous solution of 4-NP (2.5 ml; Merck, Germany) (0.13 mM) was mixed with 0.5 ml of freshly prepared aqueous solution of sodium borohydride (0.1 M), and a yellow mixture was obtained. To the above solution, an appropriate amount of catalyst was added to start reduction, and the solution was quickly subjected to UV-vis measurements. During the reaction, the mixture was continuously stirred and the progress of the reaction was recorded in situ with a time interval of 60 s. The initially obtained data are assigned to the reaction start time, $t = 0$. The reaction was considered complete when the solution became colorless. The rate constant of the reduction process was determined by measuring the change in absorbance at 400 nm as a function of time.

In the case of reduction tests in simulated sea water, the solution was prepared by the dissolution of 3.6 g of simulated sea water (Merck, Germany) in 100 ml of deionized water. In this stock solution, 3.6 mg of 4-NP was dissolved and a yellow solution was obtained. The reduction process was carried out at a temperature of 5°C. The methodology of reduction was the same as described above.

To study the reusability of the catalyst, the reduction reaction was repeated 25 times. After each cycle, the catalyst was recovered by filtration, washed several times with water, and dried in air. For comparison, the catalytic activity of a carbon-based scaffold with the same quantity of catalyst was measured in the same experimental conditions as those described above.

Calculation of reduction kinetics

Because the concentration of NaBH₄ was much higher than that of 4-NP, it can be considered to have remained constant throughout the reaction. Accordingly, the reaction was considered as corresponding to a pseudo-first-order reaction model with respect to the concentration of 4-NP, and the reaction constant (k) was calculated from Eq. 3

$$\ln\left(\frac{C_t}{C_0}\right) = -kt \quad (3)$$

where C_t is the concentration of 4-NP at the specified time t , C_0 is the initial concentration, and k is the first-order rate constant (s⁻¹).

SUPPLEMENTARY MATERIALS

Supplementary material for this article is available at <http://advances.sciencemag.org/cgi/content/full/5/10/eaax2805/DC1>

Note S1. Purification of spongin, carbonization procedure, and description of in situ monitoring of carbonization process.

Note S2. Scanning electron microscopy (SEM).

Note S3. BET specific surface area measurements.

Note S4. XRD analysis.

Note S5. Description of compressive strength measurements.

Note S6. ¹³C solid-state NMR measurements.

Note S7. Raman spectroscopy of carbonized spongin.

Note S8. XPS measurements.

Note S9. NEXAFS measurements.

Note S10. Raman spectroscopy of electroplated carbonized spongin.

Note S11. XPS of electroplated carbonized spongin.

Note S12. For Fig. 5.

Note S13. Catalytic activity of CuCSBC.

Note S14. Calculation of thermodynamic parameters.

Note S15. Resistance to poisoning.

Note S16. Influence of the chemical composition of the catalyst on its catalytic properties.

Fig. S1. Cultivated *H. communis* bath sponges can be unique sources for 3D spongin scaffolds with diameters of up to 70 cm.

Fig. S2. Monitoring of the selected spongin scaffold carbonization in the temperature range between 25° and 1200°C in an argon atmosphere.

Fig. S3. Parameters of the porous structure of native and carbonized spongin.

Fig. S4. Mechanical properties of native and carbonized spongin.

Fig. S5. TEM micrographs of ultramicrotomy of nonstained, naturally occurring collagen-based spongin fiber.

Fig. S6. ¹³C solid-state NMR analysis of carbonized spongin.

Fig. S7. Impact of carbonization temperature on the carbonized spongin scaffold visualized by Raman spectroscopy.

Fig. S8. Impact of carbonization temperature on carbonized spongin scaffold visualized by XPS.

Fig. S9. SEM images of the 3D carbonized scaffold with nanoporous surface after electroplating with copper and following sonication for 1 hour.

Fig. S10. Raman spectrum of copper layers deposited on spongin carbonized at 1200°C.

Fig. S11. XPS analysis of carbonized spongin before and after metallization.

Fig. S12. Reduction of 4-NP without heterogenic catalyst.

Fig. S13. Catalytic performance of CuCSBC.

Fig. S14. Thermodynamics of the 4-NP to 4-AP transformation reaction in the presence of CuCSBC.

Fig. S15. Catalytic behavior of nonmodified carbonized spongin.

Table S1. Microstructure parameters of turbostratic graphite as used in the model reported by Dopita *et al.* (22).

Table S2. Position, intensity ratio of D and G Raman bands, and calculated nanocrystallite size L_a of spongin carbonized at different temperatures.

Table S3. Comparison of catalytic activity using non-noble metal catalysts.

Table S4. Calculated thermodynamic parameters of 4-NP reduction using CuCSBC.

References (44–76)

REFERENCES AND NOTES

1. H. Ehrlich, *Extreme Biomimetics* (Springer International Publishing, 2017).
2. M. Wysokowski, I. Petrenko, A. L. Stelling, D. Stawski, T. Jesionowski, H. Ehrlich, Poriferan chitin as a versatile template for extreme biomimetics. *Polymers* **7**, 235–265 (2015).
3. T. Szatkowski, K. Kopczyński, M. Motylenko, H. Borrmann, B. Mania, M. Graś, G. Lota, V. V. Bazhenov, D. Rafaja, F. Roth, J. Weise, E. Langer, M. Wysokowski, S. Żółtowska-Aksamitowska, I. Petrenko, S. Molodtsov, J. Hubalkova, C. G. Aneziris, Y. Joseph, A. L. Stelling, H. Ehrlich, T. Jesionowski, Extreme biomimetics: A carbonized 3D spongin scaffold as a novel support for nanostructured manganese oxide(IV) and its electrochemical applications. *Nano Res.* **11**, 4199–4214 (2018).
4. T. Jesionowski, M. Normann, S. Żółtowska-Aksamitowska, I. Petrenko, Y. Joseph, H. Ehrlich, Marine spongin: Naturally prefabricated 3D scaffold-based biomaterial. *Mar. Drugs* **16**, E88 (2018).
5. A. Soroushanova, L. N. Delgado, Z. Wu, N. Shologu, A. Kshisagar, R. Ragunath, A. M. Mullen, Y. Bayon, A. Pandit, M. Raghunath, D. I. Zeugolis, The collagen suprafamily: From biosynthesis to advanced biomaterial development. *Adv. Mater.* **31**, 1801651 (2018).

6. S. Ling, D. L. Kaplan, M. J. Buehler, Nanofibrils in nature and materials engineering. *Nat. Rev. Mater.* **3**, 18016 (2018).
7. S. Ling, W. Chen, Y. Fan, K. Zheng, K. Jin, H. Yu, M. J. Buehler, D. L. Kaplan, Biopolymer nanofibrils: Structure, modeling, preparation, and applications. *Prog. Polym. Sci.* **85**, 1–56 (2018).
8. S.-W. Chang, M. J. Buehler, Molecular biomechanics of collagen molecules. *Mater. Today* **17**, 70–76 (2014).
9. S. Ling, K. Jin, Z. Qin, C. Li, K. Zheng, Y. Zhao, Q. Wang, D. L. Kaplan, M. J. Buehler, Combining in silico design and biomimetic assembly: A new approach for developing high-performance dynamic responsive bio-nanomaterials. *Adv. Mater.* **30**, 1802306 (2018).
10. E. Taer, W. S. Mustika, R. Taslim, Synthesis of a carbon-activated microfiber from spider webs silk. *IOP Conf. Ser. Earth Environ. Sci.* **58**, 012052 (2017).
11. H. Ma, C. Li, M. Zhang, J. D. Hong, G. Shi, Graphene oxide induced hydrothermal carbonization of egg proteins for high-performance supercapacitors. *J. Mater. Chem. A* **5**, 17040–17047 (2017).
12. Y. Kawahara, N. Ishibashi, K. Yamamoto, H. Wakizaka, N. Iwashita, S. Kenjo, G. Nishikawa, Activated carbon production by co-carbonization of feathers using water-soluble phenolic resin under controlled graphitization. *Sustain. Mater. Technol.* **4**, 18–23 (2015).
13. D. Luo, B. Zhu, Z. Li, X. Qin, Y. Wen, D. Shi, Q. Lu, M. Yang, H. Zhou, Y. Liu, Biomimetic organization of a ruthenium-doped collagen-based carbon scaffold for hydrogen evolution. *J. Mater. Chem. A* **6**, 2311–2317 (2018).
14. Q. Wang, M. Jian, C. Wang, Y. Zhang, Carbonized silk nanofiber membrane for transparent and sensitive electronic skin. *Adv. Funct. Mater.* **27**, 1605657 (2017).
15. M. Lu, Y. Qian, C. Yang, X. Huang, H. Li, X. Xie, L. Huang, W. Huang, Nitrogen-enriched pseudographitic anode derived from silk cocoon with tunable flexibility for microbial fuel cells. *Nano Energy* **32**, 382–388 (2017).
16. S. Y. Cho, Y. S. Yun, S. Lee, D. Jang, K.-Y. Park, J. K. Kim, B. H. Kim, K. Kang, D. L. Kaplan, H.-J. Jin, Carbonization of a stable β -sheet-rich silk protein into a pseudographitic pyroprotein. *Nat. Commun.* **6**, 7145 (2015).
17. J. Li, Z. Ren, Y. Ren, L. Zhao, S. Wang, J. Yu, Activated carbon with micrometer-scale channels prepared from luffa sponge fibers and their application for supercapacitors. *RSC Adv.* **4**, 35789–35796 (2014).
18. M. M. R. Khan, Y. Gotoh, H. Morikawa, M. Miura, Y. Fujimori, M. Nagura, Carbon fiber from natural biopolymer *Bombyx mori* silk fibroin with iodine treatment. *Carbon* **45**, 1035–1042 (2007).
19. H. Ji, Z. Huang, X. Wu, J. Huang, Preparation, microstructure, and compressive strength of carbon foams derived from sucrose and kaolinite. *J. Mater. Res.* **29**, 1018–1025 (2014).
20. J. Sanchez-Coronado, D. D. L. Chung, Thermomechanical behavior of a graphite foam. *Carbon* **41**, 1175–1180 (2003).
21. H. Darmstadt, C. Roy, S. Kaliaguine, Characterization of pyrolytic carbon blacks from commercial tire pyrolysis plants. *Carbon* **33**, 1449–1455 (1995).
22. M. Dopita, M. Emmel, A. Solomon, M. Rudolph, Z. Matej, C. G. Aneziris, D. Rafaja, Temperature evolution of microstructure of turbostratic high melting coal-tar synthetic pitch studied using wide-angle X-ray scattering method. *Carbon* **81**, 272–283 (2015).
23. Z. Matěj, R. Kužel, L. Nichtová, XRD total pattern fitting applied to study of microstructure of TiO₂ films. *Powder Diffract.* **25**, 125–131 (2010).
24. H. Daniels, R. Brydson, B. Rand, A. Brown, Investigating carbonization and graphitization using electron energy loss spectroscopy (EELS) in the transmission electron microscope (TEM). *Philos. Mag.* **87**, 4073–4092 (2007).
25. H. O. Pierson, *Handbook of Carbon, Graphite, Diamonds and Fullerenes. Processing, Properties and Applications* (Elsevier Inc., 1994).
26. I. L. Shabalin, *Ultra-High Temperature Materials I. Carbon (Graphene/Graphite) and Refractory Metals* (Springer Netherlands, 2014).
27. P. Čapková, D. Rafaja, J. Walter, H. P. Boehm, K. F. van Malssen, Real-time X-ray diffraction study of concentration profiles in CuCl₂-intercalated graphite during deintercalation. *Carbon* **33**, 1425–1432 (1995).
28. P. Simon, X. J. Feng, M. Bobnar, P. Höhn, U. Schwarz, W. Carrillo-Cabrera, M. Baitinger, Y. Grin, Redox route from inorganic precursor Li₂C₂ to nanopatterned carbon. *ACS Nano* **11**, 1455–1465 (2017).
29. J. Engel, H. P. Bachinger, Structure, stability and folding of the collagen triple helix, in *Collagen. Topics in Current Chemistry*, J. Brinckmann, H. Notbohm, P. L. Muller, Eds. (Springer, 2005), vol. 247.
30. P. Simon, D. Grüner, H. Worch, W. Pompe, H. Lichte, T. El Khassawna, C. Heiss, S. Wenisch, R. Kniep, First evidence of octacalcium phosphate@osteocalcin nanocomplex as skeletal bone component directing collagen triple-helix nanofibril mineralization. *Sci. Rep.* **8**, 1–17 (2018).
31. A. C. Ferrari, J. Robertson, Interpretation of Raman spectra of disordered and amorphous carbon. *Phys. Rev. B* **61**, 14095–14107 (2000).
32. L. Nikiel, P. W. Jagodzinski, Raman spectroscopic characterization of graphites: A re-evaluation of spectra/structure correlation. *Carbon* **31**, 1313–1317 (1993).
33. M. F. Hochella Jr., A. H. Carim, A reassessment of electron escape depths in silicon and thermally grown silicon dioxide thin films. *Surf. Sci.* **197**, L260–L268 (1988).
34. O. V. Petrova, S. V. Nekipelov, A. E. Mingaleva, V. N. Sivkov, A. M. Obiedkov, B. S. Kaverin, K. V. Kremlev, S. Y. Kerkov, S. A. Gusev, D. V. Vyalikh, Study of composite MWCNT/pyrolytic Cr interface by NEXAFS spectroscopy. *J. Phys. Conf. Ser.* **741**, 012038 (2016).
35. B. L. Hurley, R. L. McCreery, Raman spectroscopy of monolayers formed from chromate corrosion inhibitor on copper surfaces. *J. Electrochem. Soc.* **150**, B367–B373 (2003).
36. H. Zhang, K. Taya, K. Nagaoka, M. Yoshida, G. Watanabe, 4-Nitrophenol (PNP) inhibits the expression of estrogen receptor β and disrupts steroidogenesis during the ovarian development in female rats. *Environ. Pollut.* **229**, 1–9 (2017).
37. D. J. Reish, P. Oshida, A. J. Mearns, T. C. Ginn, Effects of pollution on saltwater organisms. *Water Environ. Res.* **65**, 573–585 (1993).
38. D. Deng, X. Liao, B. Shi, Synthesis of porous carbon fibers from collagen fiber. *ChemosusChem* **1**, 298–301 (2008).
39. Z. Hasan, Y. Sik Ok, J. Rinklebe, Y. F. Tsang, D.-W. Cho, H. Song, N doped cobalt-carbon composite for reduction of *p*-nitrophenol and pendimethaline. *J. Alloys Compd.* **703**, 118–124 (2017).
40. A. P. Garcia, M. J. Buehler, Bioinspired nanoporous silicon provides great toughness at great deformability. *Comput. Mater. Sci.* **48**, 303–309 (2010).
41. A. K. Nair, A. Gautieri, S.-W. Chang, M. J. Buehler, Molecular mechanics of mineralized collagen fibrils in bone. *Nat. Commun.* **4**, 1724 (2013).
42. Z. Martin-Moldes, D. Ebrahimi, R. Plowright, N. Dinjaski, C. C. Perry, M. J. Buehler, D. L. Kaplan, Intracellular pathways involved in bone regeneration triggered by recombinant silk–silica chimeras. *Adv. Funct. Mater.* **28**, 1702570 (2017).
43. T. Lorenz, M. Bertau, F. Schmidt, L. Plass, Methanol production from CO₂, in *Methanol: The Basic Chemical and Energy Feedstock of the Future (Asinger's Vision Today)*, M. Bertau, H. Offermanns, L. Plass, F. Schmidt, H. J. Wernicke, Eds. (Springer-Verlag, 2014).
44. T. Szatkowski, M. Wysokowski, G. Lota, D. Pęziak, V. V. Bazhenov, G. Nowaczyk, J. Walter, S. L. Molodtsov, H. Stocker, C. Himcinschi, I. Petrenko, A. L. Stelling, S. Jurga, T. Jesionowski, H. Ehrlich, Novel nanostructured hematite–spongin composite developed using an extreme biomimetic approach. *RSC Adv.* **5**, 79031–79040 (2015).
45. C. Voigt, J. Storm, M. Abendroth, C. G. Aneziris, M. Kuna, J. Hubalkova, The influence of the measurement parameters on the crushing strength of reticulated ceramic foams. *J. Mater. Res.* **28**, 2288–2299 (2013).
46. T. Jawhari, A. Roid, J. Casado, Raman spectroscopic characterization of some commercially available carbon black materials. *Carbon* **33**, 1561–1565 (1995).
47. K. Kummer, V. N. Sivkov, D. V. Vyalikh, V. V. Maslyuk, A. Blucher, S. V. Nekipelov, T. Bredow, I. Mertig, M. Mertig, Oscillator strength of the peptide bond π^* resonances at all relevant x-ray absorption edges. *Phys. Rev. B* **80**, 155433 (2009).
48. G. D. Cody, H. Ade, C. M. O'D. Alexander, T. Araki, A. Butterworth, H. Fleckenstein, G. Flynn, M. K. Gilles, C. Jacobsen, A. L. D. Kilcoyne, K. Messenger, S. A. Sandford, T. Tylliszczak, A. J. Westphal, S. Wirick, H. Yabuta, Quantitative organic and light-element analysis of comet 81P/Wild 2 particles using C-, N-, and O- μ -XANES. *Meteorit. Planet. Sci.* **43**, 353–365 (2008).
49. K. Kaznacheyev, A. Osanna, C. Jacobsen, Inner-shell absorption spectroscopy of amino acids. *J. Phys. Chem. A* **106**, 3153–3168 (2002).
50. H.-K. Jeong, H.-J. Noh, J.-Y. Kim, M. H. Jin, C. Y. Park, Y. H. Lee, X-ray absorption spectroscopy of graphite oxide. *Europhys. Lett.* **82**, 67004 (2008).
51. W. Zhang, Electronic structure of aromatic amino acids studied by soft x-ray spectroscopy. *J. Chem. Phys.* **131**, 035103 (2009).
52. I. Petrenko, V. V. Zhenov, R. Galli, M. Wysokowski, J. Fromont, P. J. Schupp, A. L. Stelling, E. Niederschlag, H. Stocker, V. Z. Kutsova, T. Jesionowski, H. Ehrlich, Chitin of poriferan origin and the bioelectrometallurgy of copper/copper oxide. *Int. J. Biol. Macromol.* **104**, 1626–1632 (2017).
53. L. Debbichi, M. C. Marco de Lucas, J. F. Pierson, P. Krüger, Vibrational properties of CuO and Cu₂O₃ from first-principles calculations, and Raman and infrared spectroscopy. *J. Phys. Chem. C* **116**, 10232–10237 (2012).
54. J. P. Espinós, J. Morales, A. Barranco, A. Caballero, J. P. Holgado, A. R. González-Elipse, Interface effects for Cu, CuO, and Cu₂O deposited on SiO₂ and ZrO₂. XPS determination of the valence state of copper in Cu/SiO₂ and Cu/ZrO₂ catalysts. *J. Phys. Chem. B* **106**, 6921–6929 (2002).
55. D. Tahir, S. Tougaard, Electronic and optical properties of Cu, CuO and Cu₂O studied by electron spectroscopy. *J. Phys. Condens. Matter* **24**, 175002 (2012).
56. T. H. Fleisch, G. J. Mains, Reduction of copper oxides by UV radiation and atomic hydrogen studied by XPS. *Appl. Surf. Sci.* **10**, 51–62 (1982).
57. O. L. Krivanek, J. H. Paterson, Elms of 3d transition-metal oxides: I. Variations across the periodic table. *Ultramicroscopy* **32**, 313–318 (1990).
58. L. A. Grunes, R. D. Leapman, C. N. Wilker, R. Hoffmann, A. B. Kunz, Oxygen *K* near-edge fine structure: An electron-energy-loss investigation with comparisons to new theory for selected 3d transition-metal oxides. *Phys. Rev. B* **25**, 7157–7173 (1982).
59. Y. Q. Wang, W. S. Liang, A. Satti, K. Nikitin, Fabrication and microstructure of Cu₂O nanocubes. *J. Cryst. Growth* **312**, 1605–1609 (2010).

60. R. D. Leapman, L. A. Grunes, Anomalous $L_{3,2}$ white-line ratios in the 3D transition metals. *Phys. Rev. Lett.* **45**, 397–401 (1980).
61. R. D. Leapman, L. A. Grunes, P. L. Fejes, Study of the $L_{3,2}$ edges in the 3D transition metals and their oxides by electron-energy-loss spectroscopy with comparisons to theory. *Phys. Rev. B* **26**, 614–635 (1982).
62. G. Yang, S. Cheng, C. Li, J. Zhong, C. Ma, Z. Wang, W. Xiang, Investigation of the oxidation states of Cu additive in colored borosilicate glasses by electron energy loss spectroscopy. *J. Appl. Phys.* **116**, 223707 (2014).
63. L. Dou, Y. Wang, Y. Li, H. Zhang, Novel core-shell-like nanocomposites $x\text{Cu}@x\text{Cu}_2\text{O}/\text{MgAl}_2\text{O}_4$ through an in situ self-reduction strategy for highly efficient reduction of 4-nitrophenol. *Dalton Trans.* **46**, 15836–15847 (2017).
64. M. V. Morales, M. Rocha, C. Freire, E. Asedegbega-Nieto, E. Gallegos-Suarez, I. Rodriguez-Ramos, A. Guerrero-Ruiz, Development of highly efficient Cu versus Pd catalysts supported on graphitic carbon materials for the reduction of 4-nitrophenol to 4-aminophenol at room temperature. *Carbon* **111**, 150–161 (2017).
65. T. Wu, M. Chen, L. Zhang, X. Xu, Y. Liu, J. Yan, W. Wang, J. Gao, Three-dimensional graphene-based aerogels prepared by a self-assembly process and its excellent catalytic and absorbing performance. *J. Mater. Chem. A* **1**, 7612–7621 (2013).
66. Z. Jin, C. Liu, K. Qi, X. Cui, Photo-reduced Cu/CuO nanoclusters on TiO_2 nanotube arrays as highly efficient and reusable catalyst. *Sci. Rep.* **7**, 39695 (2017).
67. N. Sahiner, H. Ozay, O. Ozay, N. Aktas, New catalytic route: Hydrogels as templates and reactors for in situ Ni nanoparticle synthesis and usage in the reduction of 2- and 4-nitrophenols. *Appl. Catal. A Gen.* **385**, 201–207 (2010).
68. M. Nemanashi, R. Meijboom, Synthesis and characterization of Cu, Ag and Au dendrimer-encapsulated nanoparticles and their application in the reduction of 4-nitrophenol to 4-aminophenol. *J. Colloid Interface Sci.* **389**, 260–267 (2013).
69. D. Massiot, F. Fayon, M. Capron, I. King, S. Le Calve, B. Alonso, J.-O. Durand, B. Bujoli, Z. Gan, G. Hoatson, Modelling one- and two-dimensional solid-state NMR spectra. *Magn. Reson. Chem.* **40**, 70–76 (2002).
70. S. Harish, J. Mathiyarasu, K. L. N. Phani, V. Yegnaraman, Synthesis of conducting polymer supported Pd nanoparticles in aqueous medium and catalytic activity towards 4-nitrophenol reduction. *Catal. Lett.* **128**, 197–202 (2009).
71. A. Musa, M. B. Ahmad, M. Z. Hussein, M. I. Saiman, H. A. Sani, Effect of Gelatin-stabilized copper nanoparticles on catalytic reduction of methylene blue. *Nanoscale Res. Lett.* **11**, 438 (2016).
72. P. Veerakumar, S. M. Chen, R. Madhu, V. Veeramani, C. T. Hung, S. B. Liu, Nickel nanoparticle-decorated porous carbons for highly active catalytic reduction of organic dyes and sensitive detection of Hg(II) ions. *ACS Appl. Mater. Interfaces* **7**, 24810–24821 (2015).
73. C. He, Z. Liu, Y. Lu, L. Huang, Y. Yang, Graphene-supported silver nanoparticles with high activities toward chemical catalytic reduction of methylene blue and electrocatalytic oxidation of hydrazine. *Int. J. Electrochem. Sci.* **11**, 9566–9574 (2016).
74. J. M. Song, S. S. Zhang, S. H. Yu, Multifunctional $\text{Co}_{0.85}\text{Se}-\text{Fe}_3\text{O}_4$ nanocomposites: Controlled synthesis and their enhanced performances for efficient hydrogenation of *p*-nitrophenol and adsorbents. *Small* **10**, 717–724 (2014).
75. G. Sharma, P. Jeevanandam, A facile synthesis of multifunctional iron oxide@Ag core-shell nanoparticles and their catalytic applications. *Eur. J. Inorg. Chem.* **36**, 6126–6136 (2013).
76. S. Zhang, S. Gai, F. He, S. Ding, L. Li, P. Yang, In situ assembly of well-dispersed Ni nanoparticles on silica nanotubes and excellent catalytic activity in 4-nitrophenol reduction. *Nanoscale* **6**, 11181–11188 (2014).

Acknowledgments: We are grateful to J. Hubalkova for excellent technical assistance and to R. Gumeniuk and H. Stöcker for discussions and comments. **Funding:** This work was partially supported by the following research grants: DFG Grant EH 394/3 (Germany), Dr. Erich Krüger Foundation and BHMZ at TU Bergakademie Freiberg (Germany), SMWK Project 2018 no. 02010311 (Germany), DAAD-Italy Project “Marine Sponges as Sources for Bioinspired Materials Science” (no. 57397326), and Ministry of Science and Higher Education to PUT (Poland). S.Ž.-A. is grateful for support from the DAAD and Erasmus Plus programs. M.W. is thankful for financial support from Polish National Agency for Academic Exchange (PPN/BEK/2018/1/00071). M.M. would like to thank the German Research Foundation (DFG) for financial support for the subproject B2, which is a part of the Collaborative Research Centre 799 (CRC 799) “TRIP-matrix composites” project. V.S., S.N., and O.P. were supported by UD RAS (program no. 15-10-2-23), grant RFBR 19-02-00106a, the Bilateral Program of the Russian-German Laboratory at BESSY II, and the German-Russian Interdisciplinary Science Center (G-RISC) funded by the German Federal Foreign Office via the German Academic Exchange Service (DAAD). A.E. was supported by a grant from the Russian Science Foundation (no. 17-14-01089). M.K. is thankful for the financial support from Slovak grant agency APW 16-0039. Special thanks for financial support and technical assistance are given to International Institute of Biomineralogy (INTIB GmbH, Germany). **Author contributions:** I.P. and O.V. performed carbonization and electroplating experiments. C.S., M.M., and D.R. performed the XRD and EELS/HRTEM/SAED measurements and interpreted the obtained data. R.G. performed the Raman spectroscopy measurements and analyzed the data. F.R. and S.M. performed the XPS measurements and interpreted the obtained data. E.B. was responsible for ^{13}C NMR measurements. K.K. and A.R. performed the XAS measurements. O.S.P., M. Kraft, and M.B. performed SSA_{BET} measurements and analyzed the porous structure parameters. H.M. and E.N. performed the SEM imaging. S.Ž.-A., Y.J., and T.J. analyzed catalytic activity. A.E., M. Kopani, and P.S. performed HRTEM imaging of carbonized spongin. V.S., S.N., O.P., and M.W. performed the NEXAFS measurements and analyzed the data. H.E., A.P.S., and T.J. conceived and supervised the research, planned experiments, and wrote the manuscript. All of the authors discussed the results and commented on the manuscript during its preparation. **Competing interests:** The authors declare that they have no competing interests. **Data and materials availability:** All data needed to evaluate the conclusions in the paper are present in the paper and/or the Supplementary Materials. Additional data related to this paper may be requested from the authors.

Submitted 9 March 2019
Accepted 9 September 2019
Published 4 October 2019
10.1126/sciadv.aax2805

Citation: I. Petrenko, A. P. Summers, P. Simon, S. Żółtowska-Aksamitowska, M. Motylenko, C. Schimpf, D. Rafaja, F. Roth, K. Kummer, E. Brendler, O. S. Pokrovsky, R. Galli, M. Wysokowski, H. Meissner, E. Niederschlag, Y. Joseph, S. Molodtsov, A. Ereskovsky, V. Sivkov, S. Nekipelov, O. Petrova, O. Volkova, M. Bertau, M. Kraft, A. Rogalev, M. Kopani, T. Jesionowski, H. Ehrlich, Extreme biomimetics: Preservation of molecular detail in centimeter-scale samples of biological meshes laid down by sponges. *Sci. Adv.* **5**, eaax2805 (2019).

Extreme biomimetics: Preservation of molecular detail in centimeter-scale samples of biological meshes laid down by sponges

Iaroslav PetrenkoAdam P. SummersPaul SimonSonia #ó#towska-AksamitowskaMykhailo MotylenkoChristian SchimpfDavid RafajaFriedrich RothKurt KummerErica BrendlerOleg S. PokrovskyRoberta GalliMarcin WysokowskiHeike MeissnerElke NiederschlagYvonne JosephSerguei MolodtsovAlexander EreskovskyViktor SivkovSergey NekipelovOlga PetrovaOlena VolkovaMartin BertauMichael KraftAndrei RogalevMartin KopaniTeofil JesionowskiHermann Ehrlich

Sci. Adv., 5 (10), eaax2805. • DOI: 10.1126/sciadv.aax2805

View the article online

<https://www.science.org/doi/10.1126/sciadv.aax2805>

Permissions

<https://www.science.org/help/reprints-and-permissions>

Use of think article is subject to the [Terms of service](#)

Science Advances (ISSN 2375-2548) is published by the American Association for the Advancement of Science, 1200 New York Avenue NW, Washington, DC 20005. The title *Science Advances* is a registered trademark of AAAS.

Copyright © 2019 The Authors, some rights reserved; exclusive licensee American Association for the Advancement of Science. No claim to original U.S. Government Works. Distributed under a Creative Commons Attribution NonCommercial License 4.0 (CC BY-NC).